Charge-induced energy shift of a single-spin qubit under a magnetic field gradient

Kobayashi, Takashi; Noiri, Akito; Nakajima, Takashi; Takeda, Kenta; Camenzind, Leon C.; Jin, Ik Kyeong; Scappucci, Giordano; Tarucha, Seigo

DOI
10.1103/PhysRevApplied.23.054078

Publication date
2025

Document Version
Final published version

Published in
Physical Review Applied

Charge-induced energy shift of a single-spin qubit under a magnetic field gradient

Takashi Kobayashi,[1,*] Akito Noiri,[2] Takashi Nakajima,[2] Kenta Takeda,[2] Leon C. Camenzind,[2] Ik Kyeong Jin,[2] Giordano Scappucci,[3,4] and Seigo Tarucha[1,2]

[1] *RIKEN Center for Quantum Computing, Wako, Saitama 351-0198, Japan*

[2] *RIKEN Center for Emerging Matter Science, Wako, Saitama 351-0198, Japan*

[3] *QuTech, Delft University of Technology, Delft, The Netherlands*

[4] *Kavli Institute of Nanoscience, Delft University of Technology, Delft, The Netherlands*

(Received 29 August 2024; revised 6 April 2025; accepted 21 April 2025; published 28 May 2025)

An electron confined by a semiconductor quantum dot (QD) can be displaced by changes in electron occupations of surrounding QDs owing to the Coulomb interaction. For a single-spin qubit in an inhomogeneous magnetic field, such a positional displacement of the host electron results in a qubit energy shift, which must be handled carefully for high-fidelity operations. Here, we spectroscopically investigate the qubit energy shift induced by changes in charge occupations of nearby QDs for a silicon single-spin qubit in a magnetic field gradient. Between two different charge configurations of an adjacent double QD, a spin qubit shows an energy shift of about 4 MHz, which necessitates strict management of electron positions over a QD array. We confirm a correlation between the qubit frequency and the charge configuration by using a postselection analysis.

DOI: 10.1103/PhysRevApplied.23.054078

I. INTRODUCTION

Spin qubits based on silicon quantum dots (QDs) are regarded as a compelling platform for quantum information processing. Recently, milestones toward fault-tolerant quantum computation have been achieved, including fault-tolerant fidelities of universal gates [1–4], measurement and initialization [4–6], and quantum phase-error correction [7]. Efforts to scale up toward large-scale quantum information processors have spurred extensive research in various areas such as multiqubit development [6,8], high-temperature operations [4,9–11], and the adaption of industrial fabrication technologies [8,12]. In scaling up quantum processors, crosstalk effects from various sources are one of the serious obstacles [6]. Spin-qubit operations accompanied by a transfer of electrons can cause crosstalk originating from the Coulomb interaction among qubit-host electrons. This class of operations includes qubit shuttling [13–18] and midcircuit qubit measurement for feedback [4,6,19], both of which play indispensable roles in varieties of silicon-spin-based quantum architectures [20–24]. An electron transferred in such operations changes electrostatic potential in nearby QDs due to the Coulomb interaction and displaces electrons inside these QDs. This results in a Zeeman energy shift of the spin qubits hosted by the displaced electrons in the presence of an inhomogeneous magnetic field [Fig. 1(a)]. To assess the impact of the positional displacement of a qubit-host electron, the charge-induced energy shift of a spin qubit in a magnetic field gradient should be proved directly, while a charge-induced change of exchange coupling has been utilized for operations of singlet-triplet qubits previously [25–27].

A magnetic field gradient in a spin qubit device with a micromagnet [28] can make the charge-induced energy shift large enough to be a major phase-error source, although it has not yet been measured. A number of reports on qubit shuttling do not pay attention to phase accumulation on a qubit near the shuttled qubit [13–16,18]. A recent work demonstrating a two-qubit gate between a shuttled and a localized qubit also does not measure the charge-induced energy shift while dealing with phase accumulation by a decoupling pulse [17]. The charge-induced energy shift relevant to spin-to-charge conversion for qubit readout will be crucial in quantum circuits with midcircuit measurements, which are not implemented in the field of silicon spin qubits except for phase-incoherent implementations [6,19]. In singlet-triplet qubits, a charge-induced energy shift has been observed and utilized for their operations previously [25–27]. This energy shift is mainly due to the change of exchange interaction induced

*Contact author: takashi.kobayashi@riken.jp

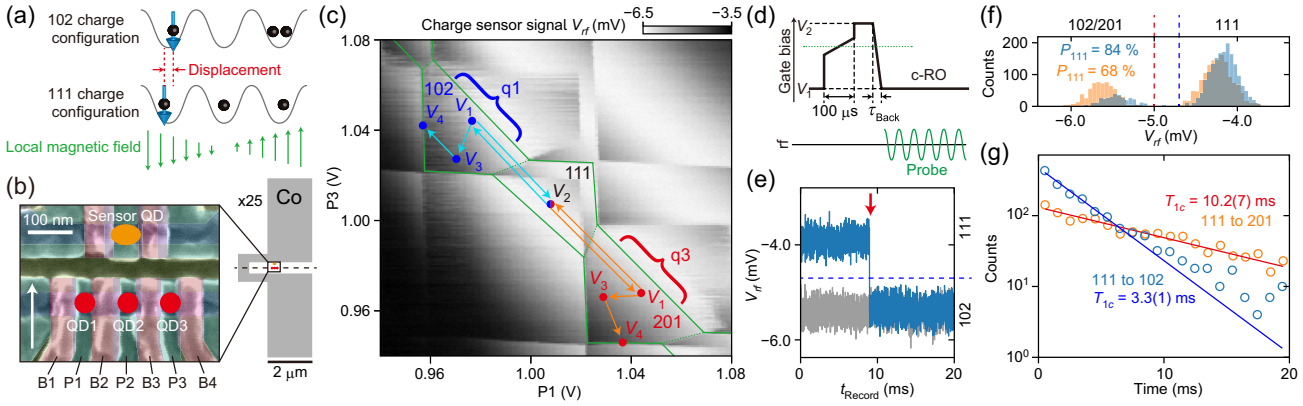

FIG. 1. Charge-preparation protocol. (a) Schematic image of the mechanism of the charge-configuration-dependent energy shift of a spin qubit. (b) SEM image of the device (left) and schematic drawing of the cobalt micromagnet (right). The red circles show QDs hosting spin qubits. The orange ellipsoid shows the QD serving as a charge sensor. The white arrow shows the direction of the external magnetic field. The black rectangle in the right-hand side panel shows the area shown in the left-hand side panel. The micromagnet has an inversion symmetric about the dashed line. (c) Charge stability diagram as a function of P1 and P3 biases. Green solid and dotted lines show the position of the charge degeneracy points relevant to QD-reservoir and inter-QD tunneling, respectively. In addition, $n_1n_2n_3$ denotes the charge configuration, giving the ground state in the region enclosed by the charge degeneracy points; V_1, V_2, V_3, and V_4 denote gate-bias sets used in the experiments. For V_1, V_3, and V_4, different bias sets are used between experiments containing q1 and q3 operations, as denoted in the figure. The bias set for V_2 is identical for both q1 and q3 experiments. (d) Sequence of gate bias (top) and rf pulses (bottom) to evaluate the charge-preparation protocol. The system prepared in the 102 and 201 regions is adiabatically transferred to the 111 region through the charge degeneracy point between the 102 and 201 regions and 111 region (green dotted line) and returned from the center of the 111 region (V_2) to the center of the 102 and 201 regions (V_1) in the pulse-back duration τ_{Back}. To evaluate the probability of obtaining the 111-charge configuration P_{111} in the 102 and 201 regions, we apply a probe-tone burst (green meandering curve) and measure reflection in the charge-readout (c-RO) stage. (e) Two typical charge-sensor signals V_{rf} as a function of time after returning to the 102 region, t_{Record}. The high and low V_{rf} values denoted by the orange and green dashed line indicate occupations of the 111 and 102 configurations, respectively. (f) Histogram of the V_{rf} value at $t_{\mathrm{Record}}=0$. Blue and orange data are measured in the 102 and 201 regions, respectively. The dashed lines show threshold values used to discriminate charge configurations. (g) Distributions of the dwell time in the 111 configuration in the 102 and 201 regions (blue and orange). The blue and red curves are exponential fit functions to evaluate the charge relaxation time T_{1c}, as shown in the figure.

by the positional displacement of an electron instead of the magnetic field gradient and, thus, would be suppressed with exchange coupling that a barrier-gate bias can control. In contrast, the charge-induced energy shift due to a magnetic field gradient is not sensitive to gate bias, as shown in this work, necessitating more careful treatment.

In this work, we report the energy shift of spin qubits induced by positional displacement of the qubit-host electrons in the presence of a magnetic field gradient. The electron position in a QD changes with the electrostatic potential. In a silicon QD, the electrostatic potential is determined by gate biases and charge configurations of nearby QDs. To distinguish and separately investigate contributions of the positional displacement of an electron induced by changes in QD charge configurations and gate biases in the qubit energy, we develop a protocol to prepare different charge configurations at an identical gate-bias set. Measuring qubit resonance frequencies by incorporating this protocol into qubit-operation sequences, we observe an energy shift of around 4 MHz between two different charge configurations at the same gate-bias condition. Measurements with changing gate biases show that this charge-induced energy shift is less sensitive to gate biases than the energy shift caused by gate bias. Finally, we confirm the correlation between the charge configuration and the qubit energy via a postselection analysis. The device is a triple-QD device made from a ^{28}Si/SiGe quantum well [Fig. 1(b), left-hand side]. The device structure is nominally identical to Refs. [1,17,29]. Voltages on the plunger gates (labeled P1, P2, and P3) predominantly change the electric potential of the QDs (i.e., QD1, QD2, and QD3) and, thus, their electron occupations (n_1, n_2, and n_3). We denote charge configurations of the triple-QD system as $n_1n_2n_3$. The pitch of the plunger gates is 90 nm. The barrier gates B1, B2, B3, and B4 are used to modify tunnel coupling between a QD and an electron reservoir (for B1 and B4) or between QDs (for B2 and B3). The barrier-gate voltages are kept constant throughout the experiments. The device is tuned to the three-electron regime as shown in the charge stability diagram in Fig. 1(c), where QD-reservoir and inter-QD degeneracy points (solid and dotted lines) separate charge-stable regions labeled by the ground-state charge configurations (102, 111, and 201). We refer to the spin qubits hosted by

electrons in QDi (i = 1, 2, 3) as qi, while q2 is not used in this work. The device is subjected to an external magnetic field of 420 mT (white arrow). A cobalt micromagnet fabricated on top of the device [Fig. 1(b), right-hand side] induces a longitudinal magnetic field gradient over the QD array. The total magnetic field increases from left to right and provides qubit energies of around 16 GHz. The QD array is nominally on the symmetry axis of the micromagnet (dashed line) to suppress the magnetic field gradient along the vertical axis. A transverse magnetic field gradient is also induced, enabling us to electrically drive spin resonance by applying microwave voltage to a gate under the plunger and barrier gates. Valley splittings in QD1, QD2, and QD3 measured by magneto-spectroscopy are 80 μeV, 100 μeV, and 90 μeV, respectively, sufficiently large to suppress the population of excited valley states. Transitions of charge configurations are manifested as sudden changes in conductance of the adjacent charge-sensor QD, which is measured via radio-frequency (rf) reflectometry [30]. A tank circuit for the reflectometry consists of a NbTiN spiral inductor with an inductance of 2.1 μH and a parasitic capacitance. We use the probe-tone frequency of 187.6 MHz. The qubit states are measured by a combination of energy-selective tunneling to a reservoir and the charge-sensing measurement [31]. The device is cooled via a dilution refrigerator with a base temperature of 30 mK while the electron temperature is 70 mK.

II. CHARGE-PREPARATION PROTOCOL

To measure the charge-induced qubit energy shift in the identical gate-bias condition, we utilize a pulse sequence to prepare the 111 configuration in the 102 and 201 charge-stable regions, as shown in Fig. 1(d) [also see Fig. 1(c) for the actual voltage sets used for V_1 and V_2]. The system is first ramped adiabatically from the 102 and 201 regions to the 111 region and then pulsed back to the 102 and 201 regions, respectively. If the pulse-back stage is nonadiabatic against the inter-QD tunnel coupling, the system remains in an excited state with the 111 configuration in the 102 or 201 region regardless of the spin state. The device is tuned to suppress the tunnel couplings between neighboring QDs, which enables us to implement the nonadiabatic passage by using a short pulse-back duration τ_{Back}. We note that the actual ramp rate is limited by low-pass filters with a cutoff frequency of 39 MHz. The passage to the 111 region is kept adiabatic by slowly ramping gate biases over a narrow range (10 mV in the P1 or P3 bias) around the inter-QD charge degeneracy point in a long duration of 100 μs.

Figure 1(e) shows two traces of charge-sensor signals V_{rf} as a function of time after returning to the 102 region t_{Record}, evaluating the charge-preparation protocol with $\tau_{\mathrm{Back}}=0$ maximizing nonadiabaticity of the pulse-back stage. The blue and gray traces are typical time traces when the 111 and 102 configurations, respectively, are loaded. The V_{rf} value higher or lower than the threshold value denoted by the dashed line indicates the occupation of the 111 or 102 configuration, respectively, at each t_{Record} value. While the threshold value is chosen artificially, the discrimination of the charge state is not sensitive to the choice by virtue of the large signal-to-noise ratio. The probability of obtaining the 111 configuration by the charge-preparation protocol P_{111} is equivalent to the probability of finding the 111 configuration at $t_{\mathrm{Record}}=0$. Figure 1(f) shows a histogram of V_{rf} at $t_{\mathrm{Record}}=0$ (blue bars). Dividing the number of counts on the V_{rf} bins higher than the threshold by the total number of experimental shots, we estimate P_{111} at 84% in the 102 region. We performed a similar experiment in the 201 region (orange bars) and obtained $P_{111}=68\%$ due to larger tunnel coupling between QD1 and QD2. The abrupt drop of the signal in the blue trace [Fig. 1(e), red arrow] indicates the relaxation from the 111 configuration to the 102 configuration. We extract the relaxation time of the 111 configuration T_{1c} from the statistics of the jump times, as shown in Fig. 1(g), finding $T_{1c}=3.3(1)$ ms in the 102 region and $T_{1c}=10.2(7)$ ms in the 201 region. The difference in T_{1c} can be explained by the variation in the QD-reservoir tunnel couplings for QD1 and QD3. Since these T_{1c} values are much longer than the spin-qubit operation time for spectroscopy (less than 100 μs), we can measure the resonance frequencies of spin qubits in the 111 configuration even in the 102 and 201 regions before the charge configuration relaxes to the ground state.

III. QUBIT SPECTROSCOPY WITH CHARGE PREPARATION

Figure 2(a) schematically shows the sequence to manipulate spin qubit q1 with the prepared charge configurations in QD2 and QD3. The q1 state is first initialized to the spin-down state in the 102 region using energy-selective tunneling between QD1 and the adjacent reservoir. Then, the 111 or 102 configuration is prepared in the 102 region. During a wait time of 30 μs, microwave pulses are applied to manipulate q1. The exchange coupling between q1 and q2 in the 111 configuration is negligibly small in the middle of the 102 region, owing to the suppression of tunnel coupling for the charge preparation. Before the energy-selective readout of the q1 state, we reset the charge configuration to 102 since the optimum readout point depends on the charge configuration. For this purpose, bringing the gate biases to V_3 in Fig. 1(c), relaxation from the 111 configuration to the 102 configuration is facilitated. This enables us to read out q1 in the 102 configuration near the 102–002 charge degeneracy point [V_4 in Fig. 1(c)] independent of the charge configuration during qubit operations. By interchanging the roles of QD1 and QD3, we also can operate q3 with the charge preparation. We implement this

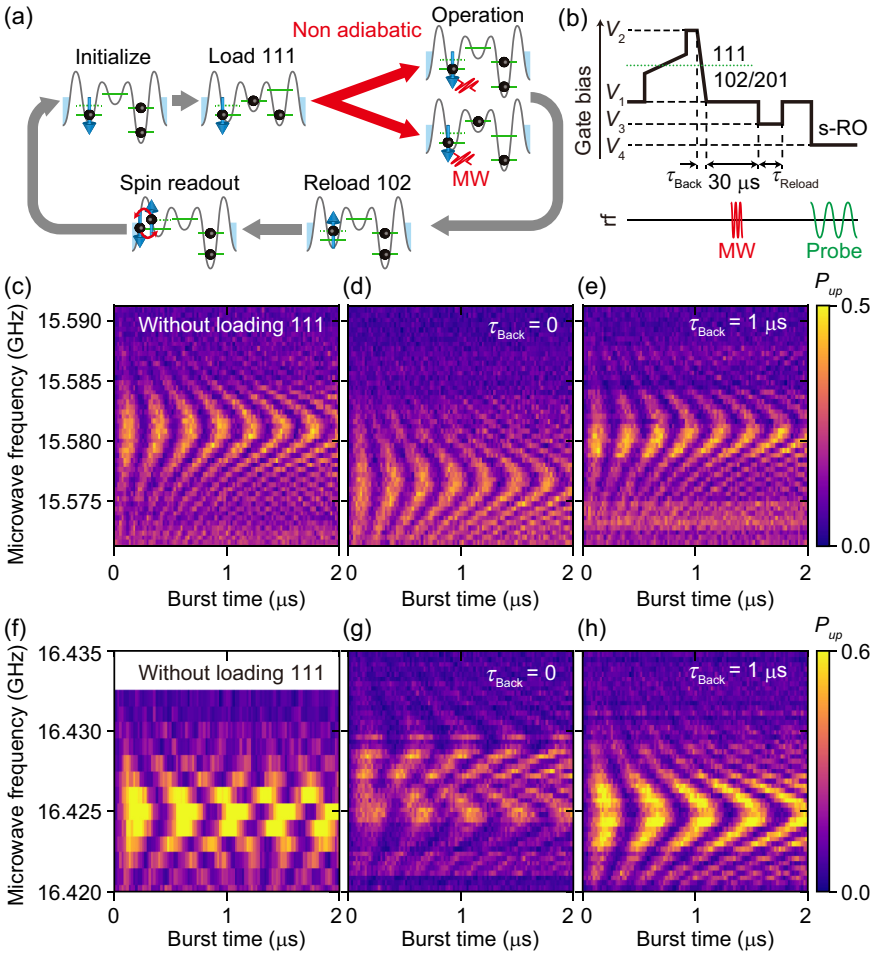

FIG. 2. Qubit spectroscopy with the charge-preparation protocol. (a) Schematic of the q1 operation sequence incorporated with the charge-preparation protocol. (b) Pulse sequence to implement the conceptual sequence in (a). The voltage sets V_1, V_2, V_3, and V_4 in the gate-bias pulse sequence are shown in Fig. 1(c). The red meandering curve in the rf pulse sequence shows microwave for qubit control. The qubit state is measured in the spin-readout (s-RO) stage at the end. (c)–(h) Spectroscopy measurements of (c)–(e) q1 and (f)–(h) q3 using a microwave burst without the charge preparation as a reference in (c) and (f), with the charge preparation using $\tau_{Back} = 0$ in (d) and (g), and $\tau_{Back} = 1$ μs in (e) and (h).

experimental sequence by the pulse sequence shown in Fig. 2(b). A reset-stage duration τ_{Reload} of 5 μs or 15 μs is used for operations of q1 or q3, respectively.

Microwave response of q1 and q3 exhibits charge-configuration dependence, as shown in Figs. 2(c)–2(h). The Rabi chevron pattern for q1 and q3 in Fig. 2(c)–(f) is taken with keeping the system in the 102 or 201 region without the charge preparation as a reference, centered around 15.581 GHz or 16.425 GHz, respectively. We observe no alias features due to the occupation of the excited valley states [32]. Figures 2(d) and 2(g) show the microwave response of q1 and q3, respectively, when the charge configurations are prepared by the maximally nonadiabatic pulse-back stage ($\tau_{Back} = 0$). The chevron pattern of q1 shifts to a lower frequency (15.577 GHz) and the q3 spectrum shows an alias feature at a higher frequency (16.429 GHz). The exchange interactions from q2 are suppressed by the small inter-QD tunnel couplings, hardly accounting for these spectra. Here, τ_{Back} of about 1 μs or longer makes the pulse-back stage adiabatic against the inter-QD tunnel coupling; the Rabi chevron patterns in the reference experiments revert with $\tau_{Back} = 1$ μs [Figs. 2(e) and 2(h)]. These results indicate that the prepared charge configuration determines the spectra. We also obtain Ramsey coherence times T_2^* of 6.9(5) μs and 7(1) μs for q1 without and with the charge-preparation protocol, respectively. These values coincide with their fitting errors, indicating the negligible impact of the charge-preparation protocol in qubit spectroscopy. The insensitivity of T_2^* to the charge-preparation protocol is explained by the long T_{1c} values and also the small positional displacement of the qubit-host electron, as discussed later.

The charge-configuration dependence of the qubit resonance frequencies is explained by the Coulomb repulsion

in the presence of the magnetic field gradient. The q1- or q3-host electron is repulsed leftward or rightward when an electron moves from QD3 or QD1 in the 102 or 201 configuration to QD2 in the 111 configuration, respectively. Since the local magnetic field increases from left to right in the current device, these repulsions by the 111 configuration should result in a negative frequency shift for q1 and a positive shift for q3 consistently with the observed frequency shifts. We estimate that the positional displacement of the electron hosting q1 is 0.9 nm using the measured frequency shift of 4 MHz and the average magnetic field gradient of 170 μT/nm. The field gradient is estimated from the difference of resonance frequencies between q1 and q3 [Figs. 2(c) and 2(f)] and the distance between QD1 and QD3 expected from the plunger-gate pitch. We compare this estimation with a simple electrostatic model. We consider the positional displacement of an electron in a harmonic potential with an orbital level spacing of $h\omega_{orb}/2\pi$ (h is the Plank constant) via the Coulomb potential from another electron fixed at a distance d. Treating the electrons as point charges, the former electron is displaced by $\Delta x(d) = e^2/4\pi\varepsilon m^* {\omega_{orb}}^2 d^2$ (e is the elementary charge, m^* is the electron effective mass, and ε is dielectric constant in silicon) for $\Delta x(d) \ll d$ in comparison with the absence of the latter electron. The electron positional displacement between the 102 and 111 configurations is expressed by $\Delta x(d) - \Delta x(2d)$. For a silicon QD with a typical orbital spacing of 1 meV and $d = 90$ nm, we obtain $\Delta x(d) - \Delta x(2d)$ at about 4 nm. Screening of the Coulomb interaction by gate electrodes may account for the discrepancy between the simple electrostatic model and the experiment.

Qubits defined in different charge configurations can be susceptive to gate biases differently, which can be probed by measuring the resonance frequencies as a function of gate biases. Figure 3(a) schematically shows the pulse sequence to measure the gate-bias dependence of the q1 resonance frequencies, where the gate bias on the qubit-operation stage (colored segment) is varied along the white arrow in Fig. 3(b) so that the energy levels in QD1 and QD2 are detuned without moving the QD2 level. For this experiment, the nonadiabaticity of the pulse-back stage is reduced by a moderate τ_{Back} value of 0.2 μs so as to populate the 102 and 111 configurations evenly. In the operation stage, we apply a Ramsey pulse sequence consisting of two $\pi/2$ pulses with a microwave frequency f_0 separated by an evolution time t_{evol} to precisely extract q1 resonance frequencies in the 102 and 111 configurations, i.e., f_{102} and f_{111}. Figure 3(c) displays the resulting Ramsey fringes as a function of the energy-level detuning. Two oscillation modes attributed to the 102 and 111 configurations are superimposed. Here, the detuning value on the perpendicular axis is indicated by the P1-bias offset from V_1 [white circle in Fig. 3(b)], i.e., ΔP1. By fitting a function $A_1\exp[-(t_{\mathrm{evol}}/{T_2}^*)^2]\cos[2\pi\delta_1 t_{\mathrm{evol}} + \phi_1] + A_2\exp[-(t_{\mathrm{evol}}/{T_2}^*)^2]\cos[2\pi\delta_2 t_{\mathrm{evol}} + \phi_2] + B$ to the Ramsey fringes at each ΔP1, we obtain the oscillation frequencies δ_1 and δ_2 corresponding to $|f_{102}-f_0|$ or $|f_{111}-f_0|$. Combining datasets measured with $f_0 = 15.582$ GHz [Fig. 3(c)], 15.575 GHz, and 15.572 GHz (not shown), we reconstruct the ΔP1 dependence of f_{102} and f_{111} from δ_1 and δ_2, as shown in Fig. 3(d).

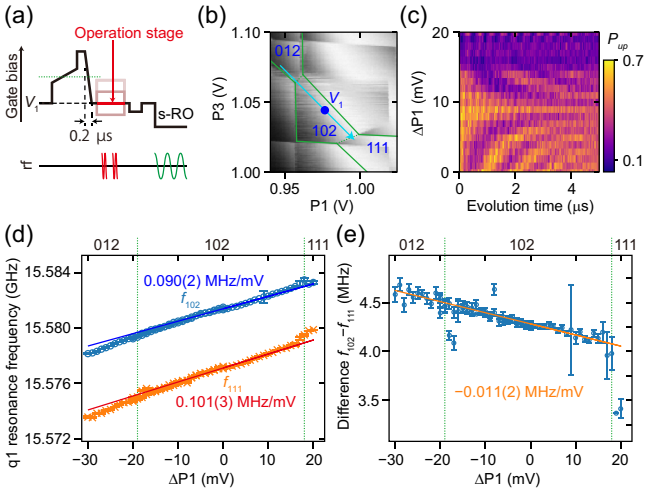

FIG. 3. Detuning dependence of q1 resonance frequencies. (a) Pulse sequence to measure the detuning dependence. Voltage in the operation stage (colored segment) is changed in the experiment. During this segment, two microwave pulses for the Ramsey interferometry are applied to q1. We used τ_{Back} of 0.2 μs. (b) A magnification of the charge stability diagram in Fig. 1(c) around the 102 region. The cyan arrow shows the axis of energy-level detuning between QD1 and QD2, and the blue circle shows its origin corresponding to V_1 in Fig. 1(c). The green dotted lines show the 012–102 and 102–111 charge degeneracy points. (c) Spin-up probability P_{up} obtained from the Ramsey interferometry as a function of detuning. Detuning is indicated by variation of the P1 gate bias from V_1, i.e., ΔP1. The microwave frequency is fixed at 15.582 GHz. (d) Resonance frequency in the 102 and 111 configuration f_{102} and f_{111} plotted as the blue and orange symbols, respectively. The linear fit curves for f_{102} and f_{111} are shown by the blue and red solid lines, respectively, whose slopes are denoted by the same-colored numbers. The detuning range is separated into the 012, 102, and 111 regions, as denoted above the top axis. The left- and right-hand side dotted lines show the ΔP1 values at the 012–102 and 102–111 charge degeneracy points, respectively. (e) Detuning dependence of the frequency difference f_{102}–f_{111} (blue symbols). The solid line shows the linear fit curve for f_{102}–f_{111}, having a slope of −0.011(2) MHz/mV, as denoted in the figure.

The q1 resonance frequencies depend on the QD level, detuning almost linearly in both charge configurations. We attribute this dependence to positional displacement of the qubit-host electron by gate biases. In the detuning range between the 012–102 and 102–111 charge degeneracy points (dotted lines), f_{102} and f_{111} are effectively fitted by linear functions with slopes of 0.090(2) MHz/mV (blue

line) and 0.101(3) MHz/mV (red line), respectively. Similar slopes indicate small gate-bias sensitivity in the charge-induced energy shift. A residual detuning dependence appears in a frequency difference $f_{102}-f_{111}$ [Fig. 3(e)]. While the difference almost stays within the range between 4.0 MHz and 4.5 MHz in the 102 region, we obtain a slope of −0.011(2) MHz/mV via a linear fit (orange line). This small detuning dependence can be attributed to the quadraticity of the magnetic field induced by the micromagnet [33,34] or a change in the positional displacement of the q1-host electron. We note that the linear dependence of f_{102}–f_{111} over a wide range of ΔP1 implies a negligible contribution of exchange interaction between electron spins in QD1 and QD2. We can also measure f_{102} and f_{111} in the 012 and 111 regions owing to the suppressed tunnel couplings. Here, f_{102} and f_{111} change with ΔP1 near the 102–111 transition sharply, which could be due to the change in charge distribution over QD2 and QD3 induced by the inter-QD tunnel coupling.

We find that the gate biases and the charge configuration contribute to the qubit energy and the single-electron level differently. On one hand, over the ΔP1 range of 40 mV, f_{102} and f_{111} change by about 4 MHz. On the other hand, the same ΔP1 range shifts the single-electron energy level of QD1 by about 3 meV. The difference in the inter-QD Coulomb interaction between the 102 and 111 configurations, which induces a comparable qubit energy shift (about 4 MHz), shifts the single-electron energy level of QD1 by 0.4 meV, estimated from the charge stability diagram. This comparison indicates that the inter-QD Coulomb interaction can shift the q1 resonance frequency strongly even if it shifts the single-electron level weakly. This is presumably because the Coulomb interaction moves electrons along the direction of the magnetic field gradient more effectively than the plunger-gate biases in the present device. Qubit operations accompanied by electron transfers require an assessment of the impact of the Coulomb interaction on the surrounding qubits, as it could be larger than expected from a shift of single-electron levels observed in a charge stability diagram.

IV. CORRELATION BETWEEN CHARGE AND QUBIT FREQUENCY

We confirm the correlation between the resonance frequency and the charge configuration by postselecting single-shot qubit-measurement outcomes according to charge-measurement outcomes. Figure 4(a) schematically shows a pulse sequence to perform the postselection. To read out the charge configuration in addition to the qubit readout, the charge-sensor signal is recorded for 25 μs after the qubit operations, with an interim wait time of 25 μs. The Ramsey interferometry of q3 using this

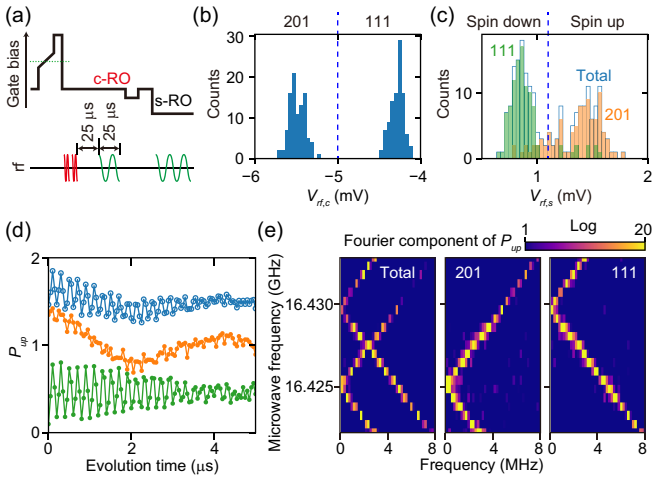

FIG. 4. Ramsey interferometry of q3 with postselection according to the charge configuration. (a) Pulse sequence for the experiment. A probe-tone pulse for an additional charge-readout stage (c-RO in red) is inserted between the second microwave pulse and the charge reset stage. (b),(c) Histograms of the single-shot charge- and qubit-readout signals, $V_{rf,c}$ and $V_{rf,s}$. $V_{rf,c}$ is an averaged value of the charge-sensor signal V_{rf} for 25 μs and $V_{rf,s}$ is a peak-to-peak value of V_{rf} over the qubit-readout duration. The dashed lines in (b) and (c) show the threshold values used to assign the charge- and qubit-readout signals to the outcomes denoted above the top axes. The blue bars in (c) show the total qubit-readout signals. Orange and green bars are subsets of the total signal postselected on the charge-readout outcome of the 201 and 111 configurations, respectively. (d) Typical Ramsey fringes without postselection (blue) and with postselection on the 201 and 111 configurations (orange and green). The microwave frequency is 16.425 GHz. (e) Fourier transformed Ramsey fringes without postselection (left panel) and with postselection on the 201 and 111 configurations (center and right panels).

sequence is performed with the charge-preparation protocol. While the nonadiabaticity of the pulse-back stage is maximized with $\tau_{\mathrm{Back}}=0$, both the 111 and 201 configurations are evenly loaded as expected from the moderate P_{111} value in Fig. 2(f), which is preferable to measure the correlation. The single-shot charge- and qubit-readout signals, $V_{rf,c}$ and $V_{rf,s}$, are shown in the form of histograms in Figs. 4(b) and 4(c), respectively. The single-shot charge- and qubit-readout signals are assigned to the 201 and 111 configurations (spin-up and spin-down states) as shown at the top of the figure using a threshold value denoted by the dashed line. Using the charge-readout outcomes, we postselect qubit-readout outcomes to calculate the spin-up probability P_{up} corresponding to the 201 and 111 configurations (orange and green bars).

The postselection reveals the correlation between the qubit resonance frequency and the charge configuration. Figure 4(d) shows Ramsey fringes obtained from the datasets with and without the postselection. Without the

postselection (blue), P_{up} shows superimposed oscillations with slow and fast frequencies. These oscillation modes separately appear in P_{up} with the postselection on the 201 and 111 configurations (orange and green). This isolation is more obvious in the Fourier transform spectra of the Ramsey fringes measured with changing the microwave frequency [Fig. 4(e)]. While two funnels centered at different microwave frequencies appear in the spectrum without the postselection (left-hand side panel), they are greatly isolated in the spectra with the postselections (middle and right-hand side panels). As the center of the funnels corresponds to the resonance frequency, these spectra prove the correlation between the resonance frequency and the charge configuration. The postselection analysis according to the charge state may be useful for calibrating the operations of qubits that undergo a change in charge configurations for proximity QDs.

V. DISCUSSION

Here, we discuss phase accumulation due to the charge-induced energy shift in important operations accompanied by electron transfers, that is, qubit shuttling and spin-to-charge conversion. Given that an electron near a qubit transfer from one QD to another QD and dwells for a time τ, the charge-induced energy shift of the qubit ΔE results in a phase accumulation of $2\pi\tau\Delta E/h$ (h is the Planck constant). This phase shift can be canceled by applying a phase gate virtually [1–4,6,7,17,29] if phase accumulation accompanied by the electron transfer can be measured for calibration in advance. This is the case of qubit shuttling [17]. Even in this case, the deviation of τ from the calibration experiment in the actual operation, $\Delta\tau$, still causes uncanceled phase accumulation of $2\pi\Delta\tau\Delta E/h$. Besides the inaccuracy of control electronics, such as timing jitters of arbitrary waveform generators, QD-level fluctuations due to, for example, two-level fluctuators in qubit devices can result in finite $\Delta\tau$ since they vary the timings of electron transfers shot by shot. For the adiabatic electron transfer between QDs having the interdot tunnel coupling of t_c, the velocity to ramp the energy-level detuning between v of the QDs has to be much slower than $(\pi t_c)^2/h$ [35]. Using this velocity, the minimum $\Delta\tau$ value for the adiabatic transfer can be represented as $\Delta\tau = \sigma_\varepsilon/v$, where σ_ε is the detuning noise amplitude. For $t_c \approx 100$ μeV [16,17] and $\sigma_\varepsilon \approx 1$ μeV [36], the minimum $\Delta\tau$ value is estimated at 40 fs. Assuming $\Delta E/h$ of 4 MHz, as observed in this work, $\Delta\tau$ of 4 ps is two orders of magnitude longer than the minimum value, for example, results in an excess phase of 50 μrad, which is sufficiently small to achieve high control fidelities [29]. We note that this origin of timing jitters increases $\Delta\tau$ toward an obstacle in high-fidelity operations for smaller t_c.

We expect the spin-to-charge conversion for qubit readout [31,37] to be more problematic than qubit shuttling. To measure the converted charge state, it must remain for around 1 μs, which corresponds to τ for this case. We note that the spin-to-charge conversion transfers an electron according to the spin quantum state before conversion. To apply this operation for the readout, previous knowledge about the spin state before the conversion is not available and, thus, a virtual phase gate cannot be calibrated to cancel an accumulated phase in contrast to the qubit shuttling where the charge configuration is deterministically controlled. To deal with such a stochastic electron transfer, unconditional phase cancelation by a refocusing pulse, as proposed in Ref. [5], will be necessary.

Finally, we assess the impact of the complexity of the quantum-processor architectures in the cancelation of the accumulated phase due to the charge-induced energy shift. In principle, each of the possible charge configurations in QDs around a spin qubit may cause a different charge-induced energy shift. Two-dimensional QD arrays, where each QD has more QDs in the vicinity than one-dimensional QD arrays, will show more energy levels due to the charge-induced energy shift. Nevertheless, the complexity of the charge-induced energy shift may not affect the phase-cancelation techniques discussed here. The virtual phase gate is calibrated according to the phase difference between the before and after operations accumulating phase, which is independent of the number of energy shifts involved in the operations. A refocusing pulse is also independent of the details of the energy shifts as long as they are reproduced before and after the refocusing pulse. Thus, the complexity of the energy shifts themselves does not hamper the cancelation of the accumulated charge, providing that the electron transfers are managed effectively. However, difficulties in the strict management of electron transfers may increase with the number of QDs surrounding a qubit.

VI. CONCLUSIONS

In conclusion, we have demonstrated spectral measurements of silicon spin qubits while preparing the charge configuration. We observe spectral shifts attributed to the positional displacement of qubit-host electrons under a magnetic field gradient. The resonance-frequency shift induced by different charge configurations is around 4 MHz, which can cause a large phase accumulation in qubit operations accompanied by electron transfers. The correlation between the charge configuration during the qubit operation and the resonance frequency is confirmed via a postselection analysis. These results reveal the impact of the charge configuration of QDs surrounding a spin qubit utilizing a magnetic field gradient.

ACKNOWLEDGMENTS

This work was supported financially by JST Moonshot Research and Development Program (Grant No. JPMJMS

226B) and JSPS KAKENHI (Grants No. 22H01160 and No. 23H05455). A.N. acknowledges support from JST PRESTO (Grant No. JPMJPR23F8). T.N. acknowledges support from JST PRESTO (Grant No. JPMJPR2017). L.C.C. acknowledges support from a Swiss NSF Mobility Fellowship (Grant No. P2BSP2 200127). We thank Kazumasa Makise for fabricating the NbTiN spiral inductor.

DATA AVAILABILITY

The data that support the findings of this article are openly available [38].

[1] A. Noiri, K. Takeda, T. Nakajima, T. Kobayashi, A. Sammak, G. Scappucci, and S. Tarucha, Fast universal quantum gate above the fault-tolerance threshold in silicon, Nature **601**, 338 (2022).

[2] X. Xue, M. Russ, N. Samkharadze, B. Undseth, A. Sammak, G. Scappucci, and L. M. K. Vandersypen, Quantum logic with spin qubits crossing the surface code threshold, Nature **601**, 343 (2022).

[3] A. R. Mills, C. R. Guinn, M. J. Gullans, A. J. Sigillito, M. M. Feldman, E. Nielsen, and J. R. Petta, Two-qubit silicon quantum processor with operation fidelity exceeding 99%, Sci. Adv. **8**, eabn5130 (2022).

[4] J. Y. Huang, R. Y. Su, W. H. Lim, M. Feng, B. van Straaten, B. Severin, W. Gilbert, N. D. Stuyck, T. Tanttu, S. Serrano, *et al.*, High-fidelity spin qubit operation and algorithmic initialization above 1K, Nature **627**, 772 (2024).

[5] K. Takeda, A. Noiri, T. Nakajima, L. C. Camenzind, T. Kobayashi, A. Sammak, G. Scappucci, and S. Tarucha, Rapid single-shot parity spin readout in a silicon double quantum dot with fidelity exceeding 99%, npj Quantum Inf. **10**, 22 (2024).

[6] S. G. J. Philips, M. T. Mądzik, S. V. Amitonov, S. L. de Snoo, M. Russ, N. Kalhor, C. Volk, W. I. L. Lawrie, D. Brousse, L. Tryputen, *et al.*, Universal control of a six-qubit quantum processor in silicon, Nature **609**, 919 (2022).

[7] K. Takeda, A. Noiri, T. Nakajima, T. Kobayashi, and S. Tarucha, Quantum error correction with silicon spin qubits, Nature **608**, 682 (2022).

[8] S. Neyens, O. K. Zietz, T. F. Watson, F. Luthi, A. Nethwewala, H. C. George, E. Henry, M. Islam, A. J. Wagner, F. Borjans, *et al.*, Probing single electrons across 300-mm spin qubit wafers, Nature **629**, 80 (2024).

[9] C. H. Yang, R. C. C. Leon, J. C. C. Hwang, A. Saraiva, T. Tanttu, W. Huang, J. Camirand Lemyre, K. W. Chan, K. Y. Tan, F. E. Hudson, *et al.*, Operation of a silicon quantum processor unit cell above one kelvin, Nature **580**, 350 (2020).

[10] L. Petit, H. G. J. Eenink, M. Russ, W. I. L. Lawrie, N. W. Hendrickx, S. G. J. Philips, J. S. Clarke, L. M. K. Vandersypen, and M. Veldhorst, Universal quantum logic in hot silicon qubits, Nature **580**, 355 (2020).

[11] L. C. Camenzind, S. Geyer, A. Fuhrer, R. J. Warburton, D. M. Zumbühl, and A. V. Kuhlmann, A hole spin qubit in a fin field-effect transistor above 4 kelvin, Nat. Electron. **5**, 178 (2022).

[12] A. M. J. Zwerver, T. Krähenmann1, T. F. Watson, L. Lampert, H. C. George, R. Pillarisetty, S. A. Bojarski, P. Amin, S. V. Amitonov, J. M. Boter, *et al.*, Qubits made by advanced semiconductor manufacturing, Nat. Electron. **5**, 184 (2022).

[13] T. A. Baart, M. Shafiei, T. Fujita, C. Reichl, W. Wegscheider, and L. M. K. Vandersypen, Single-spin CCD, Nat. Nanotechnol. **11**, 330 (2016).

[14] A. M. J. Zwerver, S. V. Amitonov, S. L. de Snoo, M. T. Mądzik, M. Rimbach-Russ, A. Sammak, G. Scappucci, and L. M. K. Vandersypen, Shuttling an electron spin through a silicon quantum dot array, PRX Quantum **4**, 030303 (2023).

[15] T. Fujita, T. A. Baart, C. Reichl, W. Wegscheider, and L. M. K. Vandersypen, Coherent shuttle of electron-spin states, npj Quantum Inf. **3**, 22 (2017).

[16] J. Yoneda, W. Huang, M. Feng, C. H. Yang, K. W. Chan, T. Tanttu, W. Gilbert, R. C. C. Leon, F. E. Hudson, K. M. Itoh, *et al.*, Coherent spin qubit transport in silicon, Nat. Commun. **12**, 4114 (2021).

[17] A. Noiri, K. Takeda, T. Nakajima, T. Kobayashi, A. Sammak, G. Scappucci, and S. Tarucha, A shuttling-based two-qubit logic gate for linking distant silicon quantum processors, Nat. Commun. **13**, 5740 (2022).

[18] I. Seidler, T. Struck, R. Xue, N. Focke, S. Trellenkamp, H. Bluhm, and L. R. Schreiber, Conveyor-mode single-electron shuttling in Si/SiGe for a scalable quantum computing architecture, npj Quantum Inf. **8**, 100 (2022).

[19] T. Kobayashi, T. Nakajima, K. Takeda, A. Noiri, J. Yoneda, and S. Tarucha, Feedback-based active reset of a spin qubit in silicon, npj Quantum Inf. **9**, 52 (2023).

[20] M. Veldhorst, H. G. J. Eenink, C. H. Yang, and A. S. Dzurak, Silicon CMOS architecture for a spin-based quantum computer, Nat. Commun. **8**, 1766 (2017).

[21] L. M. K. Vandersypen, H. Bluhm, J. S. Clarke, A. S. Dzurak, R. Ishihara, A. Morello, D. J. Reilly, L. R. Schreiber, and M. Veldhorst, Interfacing spin qubits in quantum dots and donors—hot, dense, and coherent, npj Quantum Inf. **3**, 34 (2017).

[22] J. M. Boter, J. P. Dehollain, J. P. G. van Dijk, Y. Xu, T. Hensgens, R. Versluis, H. W. L. Naus, J. S. Clarke, M. Veldhorst, F. Sebastiano, *et al.*, Spiderweb array: A sparse spin-qubit array, Phys. Rev. Appl. **18**, 024053 (2022).

[23] Z. Cai, A. Siegel, and S. Benjamin, Looped pipelines enabling effective 3D qubit lattices in a strictly 2D device, PRX Quantum **4**, 1 (2023).

[24] M. Künne, A. Willmes, M. Oberländer, C. Gorjaew, J. D. Teske, H. Bhardwaj, M. Beer, E. Kammerloher, R. Otten, I. Seidler, *et al.*, The SpinBus architecture for scaling spin qubits with electron shuttling, Nat. Commun. **15**, 4977 (2024).

[25] J. M. Taylor, H.-A. Engel, W. Dür, A. Yacoby, C. M. Marcus, P. Zoller, and M. D. Lukin, Fault-tolerant architecture for quantum computation using electrically controlled semiconductor spins, Nat. Phys. **1**, 177 (2005).

[26] M. D. Shulman, O. E. Dial, S. P. Harvey, H. Bluhm, V. Umansky, and A. Yacoby, Demonstration of entanglement of electrostatically coupled singlet-triplet qubits, Science **336**, 202 (2012).

[27] J. M. Nichol, L. A. Orona, S. P. Harvey, S. Fallahi, G. C. Gardner, M. J. Manfra, and A. Yacoby, High-fidelity entangling gate for double-quantum-dot spin qubits, npj Quantum Inf. **3**, 3 (2017).

[28] Y. Tokura, W. G. van der Wiel, T. Obata, and S. Tarucha, Coherent single electron spin control in a slanting Zeeman field, Phys. Rev. Lett. **96**, 047202 (2006).

[29] Y.-H. Wu, L. C. Camenzind, A. Noiri, K. Takeda, T. Nakajima, T. Kobayashi, C.-Y. Chang, A. Sammak, G. Scappucci, H.-S. Goan, *et al.*, Hamiltonian phase error in resonantly driven CNOT gate above the fault-tolerant threshold, npj Quantum Inf. **10**, 8 (2024).

[30] A. Noiri, K. Takeda, J. Yoneda, T. Nakajima, T. Kodera, and S. Tarucha, Radio-frequency-detected fast charge sensing in undoped silicon quantum dots, Nano Lett. **20**, 947 (2020).

[31] J. M. Elzerman, R. Hanson, L. H. Willems van Beveren, B. Witkamp, L. M. K. Vandersypen, and L. P. Kouwenhoven, Single-shot readout of an individual electron spin in a quantum dot, Nature **430**, 431 (2004).

[32] E. Kawakami, P. Scarlino, D. R. Ward, F. R. Braakman, D. E. Savage, M. G. Lagally, M. Friesen, S. N. Coppersmith, M. A. Eriksson, and L. M. K. Vandersypen, Electrical control of a long-lived spin qubit in a Si/SiGe quantum dot, Nat. Nanotechnol. **9**, 666 (2014).

[33] R. Neumann and L. R. Schreiber, Simulation of micromagnet stray-field dynamics for spin qubit manipulation, J. Appl. Phys. **117**, 193903 (2015).

[34] J. Yoneda, T. Otsuka, T. Takakura, M. Pioro-Ladrière, R. Brunner, H. Lu, T. Nakajima, T. Obata, A. Noiri, C. J. Palmstrøm, *et al.*, Robust micromagnet design for fast electrical manipulations of single spins in quantum dots, Appl. Phys. Express **8**, 084401 (2015).

[35] J. A. Krzywda and Ł Cywiński, Adiabatic electron charge transfer between two quantum dots in presence of 1/f noise, Phys. Rev. B **101**, 1 (2020).

[36] L. Kranz, S. K. Gorman, B. Thorgrimsson, Y. He, D. Keith, J. G. Keizer, and M. Y. Simmons, Exploiting a single-crystal environment to minimize the charge noise on qubits in silicon, Adv. Mater. **32**, 27 (2020).

[37] K. Ono, D. G. Austing, Y. Tokura, and S. Tarucha, Current rectification by Pauli exclusion in a weakly coupled double quantum dot system, Science **297**, 1313 (2002).

[38] T. Kobayashi, A. Noiri, T. Nakajima, K. Takeda, L. C. Camenzind, I. K. Jin, G. Scappucci, and S. Tarucha, Supporting data for 'Charge-induced energy shift of a single-spin qubit under a magnetic-field gradient', [Data set] Zenodo, 2025, https://doi.org/10.5281/zenodo.15209185.